

OVER 5,000 YEARS OF ENSEMBLE FUTURE CLIMATE SIMULATIONS BY 60-KM GLOBAL AND 20-KM REGIONAL ATMOSPHERIC MODELS

RYO MIZUTA, AKIHIKO MURATA, MASAYOSHI ISHII, HIDEO SHIOGAMA, KENSHI HIBINO, NOBUHITO MORI, OSAMU ARAKAWA, YUKIKO IMADA, KOHEI YOSHIDA, TOSHINORI AOYAGI, HIROAKI KAWASE, MASATO MORI, YASUKO OKADA, TOMOYA SHIMURA, TOSHIHARU NAGATOMO, MIKIKO IKEDA, HIROKAZU ENDO, MASAYA NOSAKA, MIKI ARAI, CHIHARU TAKAHASHI, KENJI TANAKA, TETSUYA TAKEMI, YASUTO TACHIKAWA, KHUJANAZAROV TEMUR, YOUICHI KAMAE, MASAHIRO WATANABE, HIDETAKA SASAKI, AKIO KITOH, IZURU TAKAYABU, EIICHI NAKAKITA, AND MASAHIDE KIMOTO

An unprecedentedly large ensemble of climate simulations with high-resolution atmospheric models enables the assessment of probabilistic change by global warming in low-frequency local-scale severe events.

Planning of adaptation to global warming is ready to start at the national level, presuming that warming of the climate system is unequivocal and that continued emissions of greenhouse gases will cause further warming and changes in all components of the climate system (IPCC 2013). Planning for adaptation will be based on impact assessments

of disasters, agriculture, water resources, ecosystems, human health, and so on, in each region. For each impact assessment, detailed projections of extreme events, such as heavy rainfall, heat wave, drought, and strong wind, are required at the regional scale as well as projections of climatological temperature and precipitation.

AFFILIATIONS: MIZUTA, MURATA, ISHII, IMADA, YOSHIDA, AOYAGI, KAWASE, ENDO, NOSAKA, SASAKI, AND TAKAYABU—Meteorological Research Institute, Tsukuba, Ibaraki, Japan; SHIOGAMA—National Institute for Environmental Studies, Tsukuba, Ibaraki, Japan; HIBINO, ARAKAWA, NAGATOMO, KAMAE, AND KITOH—University of Tsukuba, Tsukuba, Ibaraki, Japan; MORI, OKADA, SHIMURA, TANAKA, TAKEMI, TEMUR, AND NAKAKITA—Disaster Prevention Research Institute, Kyoto University, Uji, Kyoto, Japan; MORI, ARAI, TAKAHASHI, WATANABE, AND KIMOTO—Atmosphere and Ocean Research Institute, University of Tokyo, Kashiwa, Chiba, Japan; IKEDA—Japan

Agency for Marine-Earth Science and Technology, Yokohama, Kanagawa, Japan; TACHIKAWA—Graduate School of Engineering, Kyoto University, Kyoto, Japan

CORRESPONDING AUTHOR: Ryo Mizuta, rmizuta@mri-jma.go.jp

The abstract for this article can be found in this issue, following the table of contents.

DOI:10.1175/BAMS-D-16-0099.1

In final form 16 November 2016
©2017 American Meteorological Society

However, the uncertainty of the change is still large, even for the global-mean surface temperature change. Uncertainties become larger as the spatial scale considered is reduced, for example, when examining the regional distribution of change. There is greater uncertainty in temporally variable components than temporal-mean values. Furthermore, rare events have much larger uncertainty, although such events can have the most significant impacts on human activity (Collins et al. 2013).

The major sources of these uncertainties are uncertainties in the emission scenarios of greenhouse gases and in climate models. These are considered by phase 5 of the Coupled Model Intercomparison Project (CMIP5) experiments, in which multiple emission scenarios are applied to multiple climate models, providing information for evaluating the uncertainties in large-scale phenomena (e.g., Hawkins and Sutton 2009).

In addition, uncertainty from internal variability is expected to be more important for less frequent anomalous weather and climate extremes (Deser et al. 2012; Xie et al. 2015). Internal variability includes decadal variations in the ocean, interannual variability in the extratropical atmosphere, intraseasonal variation in the tropics, and so on. Kay et al. (2015) emphasized the importance of uncertainties in climate projections arising from internal variability by conducting a large ensemble climate simulation. Large ensemble simulations yield the probability density functions of variables such as temperature and precipitation, and allow us to discuss their changes in a warming climate, and the function tails as the climate extremes.

Large ensemble simulations are also useful for understanding human influences on past changes in extreme events, by using an approach termed probabilistic event attribution (PEA). The approach evaluates the degree to which human influence has affected the probability and magnitude of individual extreme events rather than long-term trends (Allen 2003), through comparing results from atmospheric general circulation models (AGCMs) with and without anthropogenic changes in boundary conditions during a single season or a few years (Pall et al. 2011; Christidis and Stott 2014; Mori et al. 2014; Shioyama et al. 2014). The AGCM-based PEA generally benefits from much larger initial-condition ensembles (≥ 100) than the traditional detection and attribution studies using atmosphere–ocean coupled models (AOGCMs) (< 10).

Currently, however, suites of climate change simulations by AOGCMs are conducted with an

atmospheric resolution coarser than 100 km (Collins et al. 2013), and a similar resolution in the large ensemble simulations. These resolutions are not fine enough for regional impact assessment studies related to small-scale climate extremes affected by local topography, and low-resolution models are not suitable for phenomena such as tropical cyclones, the East Asian monsoon, and blocking (e.g., Fowler et al. 2007). In Asia in particular, since the monsoon and tropical cyclones are major causes of natural hazards and also water sources, changes in these phenomena are the key issues for regional impact assessment. Direct dynamical downscaling to regional climate models (RCMs) can include the effects of regional-scale topography, but it cannot include phenomena that are not simulated in the parent GCMs (Xie et al. 2015).

To overcome these problems, we have been employing a high-resolution AGCM (Kitoh et al. 2016). Simulations of a warmer climate using an AGCM with 20-km resolution were performed (e.g., Murakami et al. 2012a), in which sea surface temperature (SST) changes from CMIP climate models are prescribed as the lower boundary conditions. In addition, finer-scale projections have been performed over the Japanese region by downscaling to a regional climate model with 5-km resolution (Kanada et al. 2012; Nakano et al. 2013). Furthermore, uncertainties from different SST changes, cumulus parameterization schemes, and emission scenarios have been examined using ensemble simulations using 60-km AGCM (Endo et al. 2012; Murakami et al. 2012b; Kitoh et al. 2016). The results of these simulations are now being used in various impact assessment studies for natural disasters, including river discharge/flooding (Duong et al. 2014), storm surge (Yasuda et al. 2014), and ocean waves (Mori et al. 2010; Shimura et al. 2015), as well as water resources, agriculture, ecosystems, and human health.

In this study, this approach using a high-resolution AGCM is applied to the evaluation of uncertainty arising from internal variability. The 60-km AGCM, which is capable of representing tropical cyclones, combined with dynamical downscaling using the 20-km RCM, which gives finer-scale heavy precipitation and topographical effects, are used to perform a large ensemble simulation. We performed 100-member simulations of the period 1951–2010 and 90-member simulations for 60 years of a warmer climate using the AGCM, and a large part of the results are downscaled with the RCM. In addition, 100-member AGCM simulations were performed for 1951–2010 without historical long-term warming

trends. These large-size and long-term ensembles of the high-resolution models facilitate analyses of long-term trends and future changes in localized rare events that cannot be represented by coarse-resolution models and small-size ensembles, although the uncertainty of the ocean internal variability cannot be examined. The simulation results are freely available for the community as a database named “Database for Policy Decision Making for Future Climate Change” (d4PDF), which is intended to be utilized for impact assessment studies.

MODELS AND METHODS. *Models.* The d4PDF consists of outputs from global warming simulations by a global atmospheric model with horizontal grid spacing of 60 km (AGCM) and from regional downscaling simulations covering the Japan area by a regional climate model with 20-km grid spacing (RCM).

The AGCM used here is the Meteorological Research Institute AGCM, version 3.2 (MRI-AGCM3.2). This model was developed based on a version of the numerical weather prediction model used operationally at the Japan Meteorological Agency (JMA 2007). We use the model with 60-km resolution, which has 640×320 grid cells, corresponding to a triangular truncation of 319 with a linear Gaussian grid (TL319) in the horizontal. The number of vertical levels is 64 (top at 0.01 hPa). The model is exactly the same as the MRI-AGCM3.2 with high resolution (MRI-AGCM3.2H) listed in the CMIP5 archive. Further details of the model and its performance can be found in Mizuta et al. (2012). Previous studies have shown that the AGCM has high skill in simulating regional-scale climate such as the geographical distribution of tropical cyclones (Murakami et al. 2012a,b) and monsoon precipitation (Endo et al. 2012), including intense rainfall associated with the East Asian summer monsoon

(Kusunoki and Mizuta 2013), as well as the global-scale climate (Mizuta et al. 2012).

The RCM downscaling simulations are performed by the Meteorological Research Institute Nonhydrostatic Regional Climate Model (NHRCM). The horizontal grid size is 211×175 , covering Japan, the Korean Peninsula, and the eastern part of the Asian continent. The NHRCM has 40 layers in the vertical. Detailed specifications of the model have been reported by Sasaki et al. (2011) and Murata et al. (2013).

Experimental settings. Three sets of experiments are performed by the AGCM: a historical climate simulation, a +4-K future climate simulation, and a nonwarming simulation. The SST, sea ice concentration (SIC), and sea ice thickness (SIT) are prescribed as the lower boundary conditions, and global-mean concentrations of greenhouse gases and three-dimensional distributions of ozone and aerosols as the external forcing. The duration of each experiment is 60 years. Each set of experiments has 90–100 ensemble members, for which the initial conditions and the lower boundary conditions are perturbed. The settings of the experiments are summarized in Table 1.

The past historical climate from 1951 to 2010 is simulated with 100 ensemble members. The observed monthly mean SST and SIC [Centennial Observation-Based Estimates of SST, version 2 (COBE-SST2); Hirahara et al. 2014] and climatological monthly SIT from Bourke and Garrett (1987) are used as the lower boundary conditions. In addition to using different initial conditions, small perturbations of SST (δ SSTs) based on SST analysis error are added to COBE-SST2 for the ensemble experiments. The details of these perturbations are described in the appendix. Global-mean concentrations of greenhouse gases [CO_2 , CH_4 , N_2O , and chlorofluorocarbons (CFCs)]

TABLE 1. Duration (yr), ensemble size, and prescribed boundary conditions of the three simulations.

	Historical simulation	+4-K future simulation	Nonwarming simulation
Duration	60 (1951–2010)	60	60 (1951–2010)
Members (GCM)	100	6×15	100
Members (RCM)	50	6×15	—
Greenhouse gases	Observed	Values at 2090 of RCP8.5	Values at 1850
Aerosols	Monthly output from MRI-CGCM	2090 output from MRI-CGCM	Sulfate, black carbon, organic carbon: values at 1850; mineral dust, sea salt: same as historical simulation
Ozone	Monthly output from MRI-CCM	2090 output from MRI-CCM	1961 output from MRI-CCM

are set to the observational values for each year. Three-dimensional distributions of ozone from the MRI Chemistry–Climate Model (MRI-CCM; Deushi and Shibata 2011) and aerosols from the MRI Coupled Atmosphere–Ocean General Circulation Model, version 3 (MRI-CGCM3; Yukimoto et al. 2012), are used.

The future climate in which the global-mean surface air temperature becomes 4 K warmer than the preindustrial climate is simulated, corresponding to that around the end of the twenty-first century under the representative concentration pathway 8.5 (RCP8.5) scenario of CMIP5. In this simulation, the amplitude of the warming is kept constant throughout the 60-yr integration. This is a different experimental setting from the so-called emission scenario simulations in which the stage of global warming is changing during the simulation period. With this experiment, we can obtain a large sample size under the same specified stage of global warming.

For the use of the +4-K simulation, climatological SST warming patterns (Δ SSTs) are added to the observational SST after removing the long-term trend component, as shown in Fig. 1. The trend component in the observations is derived as the leading empirical orthogonal function (EOF) computed from the 5-yr mean during 1951–2010, which explains most of the

observational trend. The Δ SSTs are the difference between 1991–2010 and 2080–99 in the historical and RCP8.5 experiments by the CMIP5 models. Six CMIP5 models were selected based on a cluster analysis of geographical patterns of SST changes (Mizuta et al. 2014) so that the six patterns cover the most part of the uncertainty of the patterns in all the CMIP5 models. Each pattern is multiplied by a scaling factor so as to give a global-mean surface air temperature warming of 4 K. The six models and the corresponding factors are listed in Table 2, and the six Δ SSTs are shown in Figs. 2a–f.

For each of the six Δ SSTs, 15-member ensemble experiments are conducted using different initial conditions and different δ SSTs, giving a total of 90 members. The δ SSTs are the same as those for the historical simulation. The greenhouse gases are set to the value in 2090 of the RCP8.5 scenario. The ozone and aerosol distributions are the average from 2088 to 2092 in the extended experiments with the same models as used in the historical simulation.

We also performed a nonwarming simulation, assuming that global warming has not taken place since the preindustrial climate. The same boundary conditions as the historical simulation are given, except that the long-term trend is removed. This simulation is intended for comparison with the historical

simulation for attribution studies of historical climate change. Since it also has no warming trend, it can be used for comparison with the +4-K simulation for analyses in which the effect of the warming trend within the historical simulation cannot be ignored, for example, the future change in the amplitude of the interannual temperature variability. The number of ensemble members is 100, using the same initial and boundary perturbations as the historical simulation. The baseline of the detrended SST is the average from 1900 to 1919 in which the SST warming since the preindustrial climate was not clearly observed. Greenhouse gases are set to the estimated

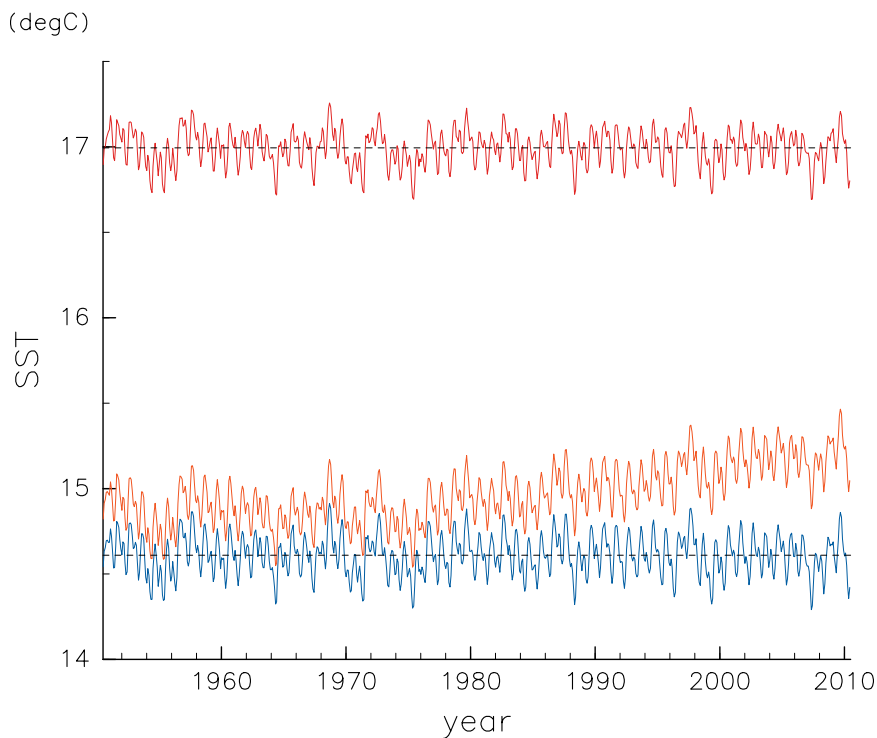


FIG. 1. Monthly mean SST averaged over 60°S–60°N prescribed for the historical climate simulation (orange line), the +4-K climate simulation (red line), and the nonwarming simulation (blue line).

TABLE 2. CMIP5 models used for obtaining SST changes, and the scaling factor multiplied by the SST difference for 1991–2010 and 2080–99. AORI = Atmosphere and Ocean Research Institute. NIES = National Institute for Environmental Studies. JAMSTEC = Japan Agency for Marine-Earth Science and Technology.

Model	Institution (Country)	Scaling factor
CCSM4	National Center for Atmospheric Research (United States)	1.10981
GFDL CM3	National Oceanic and Atmospheric Administration (NOAA) GFDL (United States)	0.75166
HadGEM2-AO	Met Office Hadley Centre (United Kingdom)	0.902224
MIROC5	AORI, NIES, JAMSTEC (Japan)	1.06162
MPI-ESM-MR	Max Planck Institute for Meteorology (Germany)	1.01852
MRI-CGCM3	Meteorological Research Institute (Japan)	1.13509

value in 1850. The ozone distribution is fixed to the average from 1960 to 1962 in the same experiment as used in the historical simulation. The aerosol is from the experiment in which the sulfate, black carbon, and organic carbon emissions are set to preindustrial values. As we cannot show much about the results of the nonwarming simulation, see Shiogama et al. (2016) for more details and the first results.

The dynamical downscaling simulations by the RCM are conducted for 50 members of the historical simulation and for 90 members of the +4-K simulation. Simulations for only 50 members are conducted for the historical case due to the limitation of the computational resource. Time integrations are split to each year; the simulation starts on 20 July and terminates on 31 August of the following year. The first 40 days of integration is the spinup, and output from 1 September to 31 August of the following year is available for diagnosis.

Climatological change and its dispersion in the results. The global-mean change in the prescribed SST from the historical simulation to the +4-K future simulation (Fig. 1) is 2.61 K. In the results of the AGCM experiments, we obtain global-mean surface air temperature change from the historical simulation to the +4-K simulation of 3.64 K. Since the observed warming from the preindustrial climate to the duration of the historical simulation (1951–2010) is 0.45 K, the warming from the preindustrial to the +4-K simulation is about 4.1 K. The error of about 0.1 K comes from the difference in land surface warming between the six CMIP5 models and the AGCM.

Figures 2g–r compare the changes in the annual-mean precipitation from the outputs of the six CMIP5 models and those from the AGCM results for the six Δ SST ensemble experiments. While all CMIP5 models (Figs. 2g–l) have precipitation increasing in the tropics and extratropics and decreasing in the subtropics, there are differences between the models associated

with the differences in the SST changes. The differences are large in the tropics, especially around the Maritime Continent. These intermodel differences are also represented in the results of the 60-km AGCM (Figs. 2m–r), showing that a certain component of the uncertainties from different climate models is covered by the six Δ SST ensemble experiments: precipitation increases more over the central to eastern equatorial Pacific and less over the Maritime Continent region in the Hadley Centre Global Environment Model, version 2—Atmosphere and Ocean (HadGEM2-AO); the Max Planck Institute Earth System Model, medium resolution (MPI-ESM-MR); and the Meteorological Research Institute Coupled Atmosphere–Ocean General Circulation Model, version 3 (MRI-CGCM3; Figs. 2i,k,l,o,q,r). This result is consistent with the El Niño-like pattern of SST change (Figs. 2c,e,f). In contrast, SST warming in the western Pacific is comparable to that in the eastern equatorial Pacific in the Community Climate System Model, version 4 (CCSM4); the Geophysical Fluid Dynamics Laboratory Climate Model, version 3 (GFDL CM3); and the Model for Interdisciplinary Research on Climate, version 5 (MIROC5; Figs. 2g,h,j,m,n,p), resulting in a more zonally uniform change in precipitation. Differences between the models are also found around the Atlantic Ocean, the Indian Ocean, the Amazon, and the South Pacific convergence zone.

BENEFITS OF THE HIGH-RESOLUTION LARGE ENSEMBLE: GCM. The high-resolution large ensemble results enable us to assess the statistical change in very rare precipitation events. Figure 3a shows the frequency distribution of daily precipitation in the historical simulation for the grid square including Tokyo, Japan, compared with the observational station data at Tokyo, without bias correction. The observational data lie within the ensemble spread of single-member results (blue lines), showing that the model simulates extreme precipitation events

very well. Since the data length is limited, in both the observations and the single-member experiment the error becomes large at a frequency lower than about 0.1% (once in 3 years). However, the frequency distribution from 10 members (green lines) can represent frequencies for a range from 0.03% (once

in 10 years) to 0.003% (once in 100 years), and the frequency distribution from the total 100 members (red line) shows reasonable frequencies around 0.001% (once in 300 years).

Figure 3b shows the change as the ratio between the historical simulation and +4-K future simulations

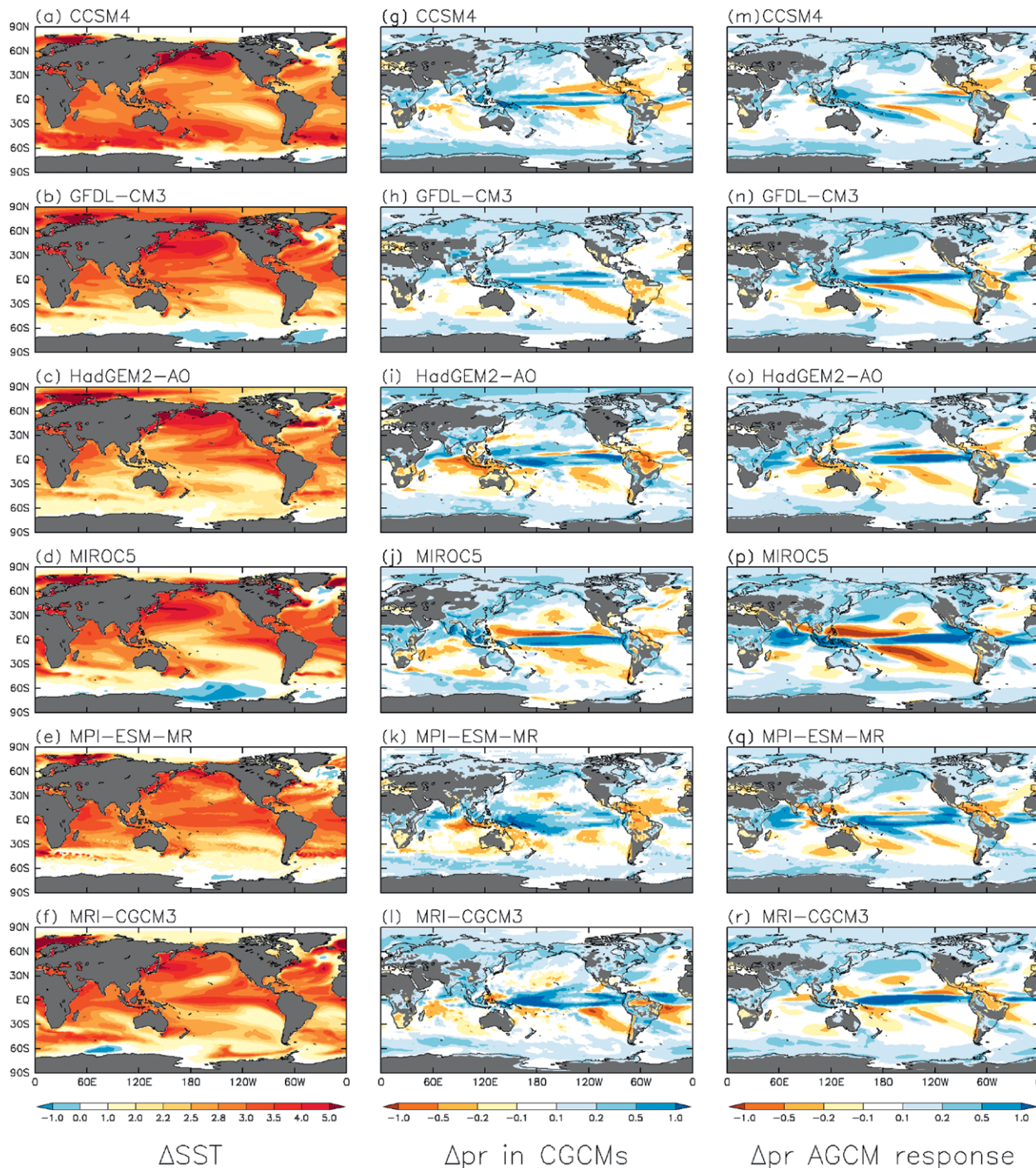


FIG. 2. Annual-mean horizontal distributions of (a)–(f) SST changes (K) for the six Δ SST ensemble experiments, (g)–(l) precipitation changes normalized by the global-mean SST change ($\text{mm day}^{-1} \text{K}^{-1}$) from the historical experiments to the RCP8.5 experiments of the six CMIP5 model outputs, and (m)–(r) those from the historical simulation to the +4-K ensemble AGCM simulation using the six different Δ SST.

of the occurrences of each precipitation rate. While the change is relatively small at weaker precipitation rates, it is positive for heavy precipitation above 70 mm day^{-1} . Moreover, the increase is larger with higher precipitation rates. Although the rates of increase depend on the prescribed SST change patterns, the increase is common to all the SST change patterns.

These results are not localized to Tokyo. Figure 4 shows the global distribution of the 10-yr return value of daily precipitation in the historical simulation and the change in the +4-K future simulation, calculated from the 90th-percentile value of the annual maximum daily precipitation. The results from a single member of the historical simulation (Fig. 4a) can capture only the large-scale features, and small-scale characteristics are masked by the noise due to the limited sample size. The change ratio obtained with a single member (Fig. 4c) consists of a mixture of regions of increasing and decreasing precipitation over most of the land. In contrast, clear and smooth images are obtained by using 90 ensemble members for each of the historical and +4-K simulations (Figs. 4b,d). The 10-yr return value of daily precipitation is over 200 mm day^{-1} in central India, the northwestern and southwestern Pacific Ocean, and the southwestern Indian Ocean. Regions of future increase are found over most of the world, and regions of future decrease are limited to the subtropics in the Atlantic and eastern Pacific

oceans. The large-scale geographical patterns of the historical simulation and the change in the warmer climate are comparable to those estimated from the CMIP5 multimodel median (Kharin et al. 2013), except for the increase over the driest regions like northern Africa and a slight decrease over the Philippines. A decrease of climatological-mean heavy precipitation over the Philippines Sea is associated with a decrease of tropical cyclone number in the future climate (Kitoh and Endo 2016). Previous studies, including Kharin et al. (2013), used fitting to extreme value distributions for estimating such extreme values, which requires assuming distribution parameters. However, the use of a large ensemble enables us to estimate extreme values without any assumptions of their distributions. The change in the global average of the return value is +32.8%. The rate of increase per 1-K warming ($11.5\% \text{ K}^{-1}$) is larger than the result from the CMIP5 multimodel median (about $5.8\% \text{ K}^{-1}$; Kharin et al. 2013), although it is within its intermodel dispersion. This could be associated with the horizontal resolution of the model (Sugiyama et al. 2010).

Figure 5a shows an unbiased estimate of the standard deviation σ_{tot} between the 90 ensemble members for the change ratio in the 10-yr return value of daily precipitation. The σ_{tot} value is $\sim 30\%$ in the subtropics and $\sim 15\%$ in the midlatitudes. The blue line in Fig. 6 is the zonal-mean ratio of the 95% confidence interval of the change ($\sim 1.96\sigma$) to the change itself

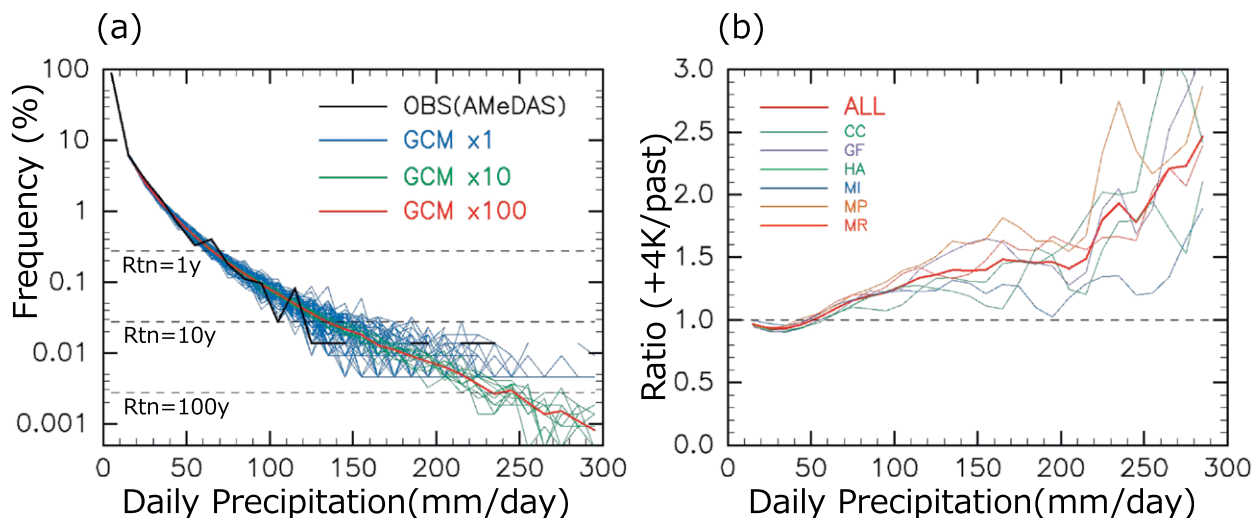


FIG. 3. (a) Frequency distributions of daily precipitation on the grid square including Tokyo for the historical simulation. The black line indicates distributions from the station observations at Tokyo from 1980 to 1999, the blue lines indicate distributions from each of the 100 ensemble members, the green lines are 10-member averages, and the red line indicates distributions from the 100 members. (b) Ratio between the historical and +4-K simulations of the occurrences of each precipitation rate on the grid square including Tokyo. The six thin lines correspond to the six ΔSST patterns, and the thick red line is from all members.

(Fig. 4d). The ratio is larger than 1 at all latitudes; that is, the confidence interval is larger than the change, meaning that uncertainty exists even regarding the sign of change. The other lines in Fig. 6 show how the statistical confidence interval of the ensemble-mean change becomes narrower as the ensemble number increases. The confidence interval for N members is calculated from 90 samples of an N -member ensemble chosen by the bootstrap method. If we use 10 members, then the sign of the change becomes confident except over the subtropics. Furthermore, the ratio decreases to less than 0.5 when the number of ensemble members is increased to 90.

The total variance σ_{tot}^2 in Fig. 5a can be decomposed into the variance due to the difference in ΔSST patterns $\sigma_{\Delta\text{SST}}^2$ (Fig. 5b) and the internal variability seen in the 15 δSST ensemble σ_{int}^2 (Fig. 5c) by using a statistical method based on a concept of the analysis of variance (ANOVA) applied by Rowell et al. (1995) and Endo et al. (2016). The result shows that $\sigma_{\Delta\text{SST}}$ is small in the extratropics (Fig. 5b), suggesting that the patterns of SST warming have less influence on this aspect of the change in the extratropics. In the equatorial Pacific and Atlantic Oceans, in contrast, the change depends

mainly on the SST warming pattern. The $\sigma_{\Delta\text{SST}}$ and σ_{int} are comparable in the subtropics, showing that the combination of the two different kinds of ensemble experiments is able to cover a wide range of uncertainty in the change.

We can also examine extreme temperature events. While such events occur more widely than extreme precipitation events, there could be some benefit in performing the high-resolution simulations around the regions affected by orography with a scale of ~ 100 km.

Figure 7a shows the global distribution of the 20-yr return value of the maximum surface air temperature in the latter half of the historical simulation. Note that this is calculated from the 95th-percentile value of annual maximum temperature, so at most one hot day is counted for each heat wave event. The values over the ocean are masked, as the day-to-day variability is smaller than in the real world due to the prescribed monthly SST. Very high temperature events over inland areas are represented. The change from the historical simulation to the +4-K simulation is shown in Fig. 7b. A large-scale distribution consistent with the CMIP5

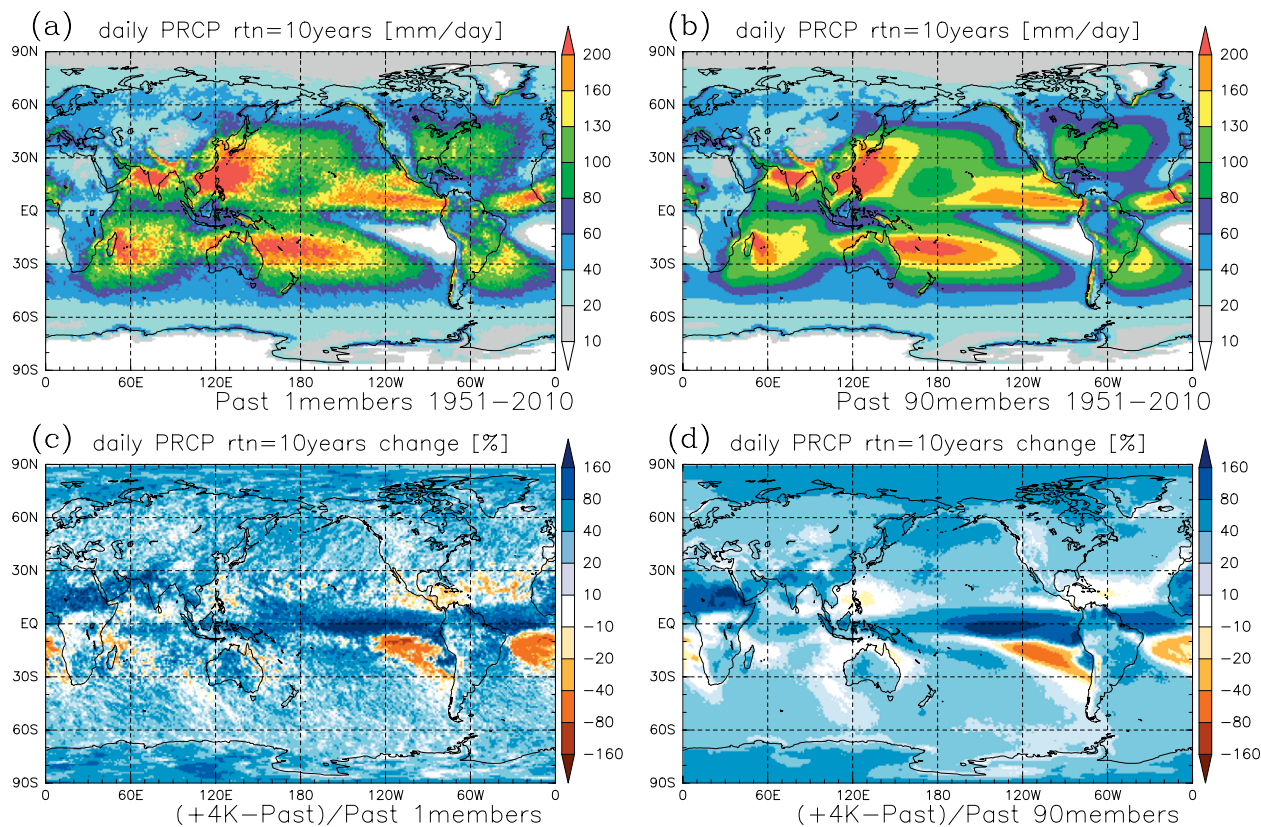


FIG. 4. The 10-yr return value of daily precipitation (a),(b) in the historical simulation and (c),(d) in the change ratio from the historical simulation to the +4-K simulation. (a),(c) The results from a single member and (b),(d) the ensemble mean of 90 members.

FIG. 5. Standard deviation σ_{tot} (%) of the differences between the historical and +4-K simulations in the 10-yr return value of daily precipitation for (a) all ensemble members, and components of σ_{tot} due to (b) the difference in ΔSST patterns $\sigma_{\Delta\text{SST}}$ and (c) the internal variability seen in the 15 δSST ensembles σ_{int} , using ANOVA without replication.

multimodel results (Collins et al. 2013; Kharin et al. 2013) is obtained over land, accompanied by a finer-scale distribution. A comparison with the seasonal-mean surface temperature warming (Figs. 7c,d) shows that the change in extremely high temperatures is almost the same as the change in the mean temperatures during the warm season over large areas of the land, with the difference being within 1 K. However, there are some exceptional areas around central Europe, southern Brazil, southern China, and the polar region, where the difference between the mean temperature warming and the extremely high temperature increase is more than 2 K. The difference in Europe is also found in an ensemble of 15 regional climate simulations over Europe (Vautard et al. 2014).

Figure 8 shows the probability distribution functions (PDFs) of annual maximum surface temperature for four representative locations. Over most of the world, the shape of the PDF does not change between the three simulations, as in Denver, Colorado (Fig. 8a). On the other hand, around central Europe and southern Brazil, as in Munich, Germany (Fig. 8b), and Rio de Janeiro, Brazil (Fig. 8c), the PDFs in the +4-K simulation are much broader than those in the historical simulation. Since the mean increase in annual maximum temperature is not so different from the increase in seasonal-mean temperature, the difference between the mean temperature warming and the extremely high temperature increase is attributed to a change in the shape of the PDFs. More elaborate analysis is needed to examine the mechanism associated with these extremely high temperature events and whether this projection is realistic. There are also some regions, such as Fairbanks, Alaska (Fig. 8d), where the shape of the PDF narrows slightly.

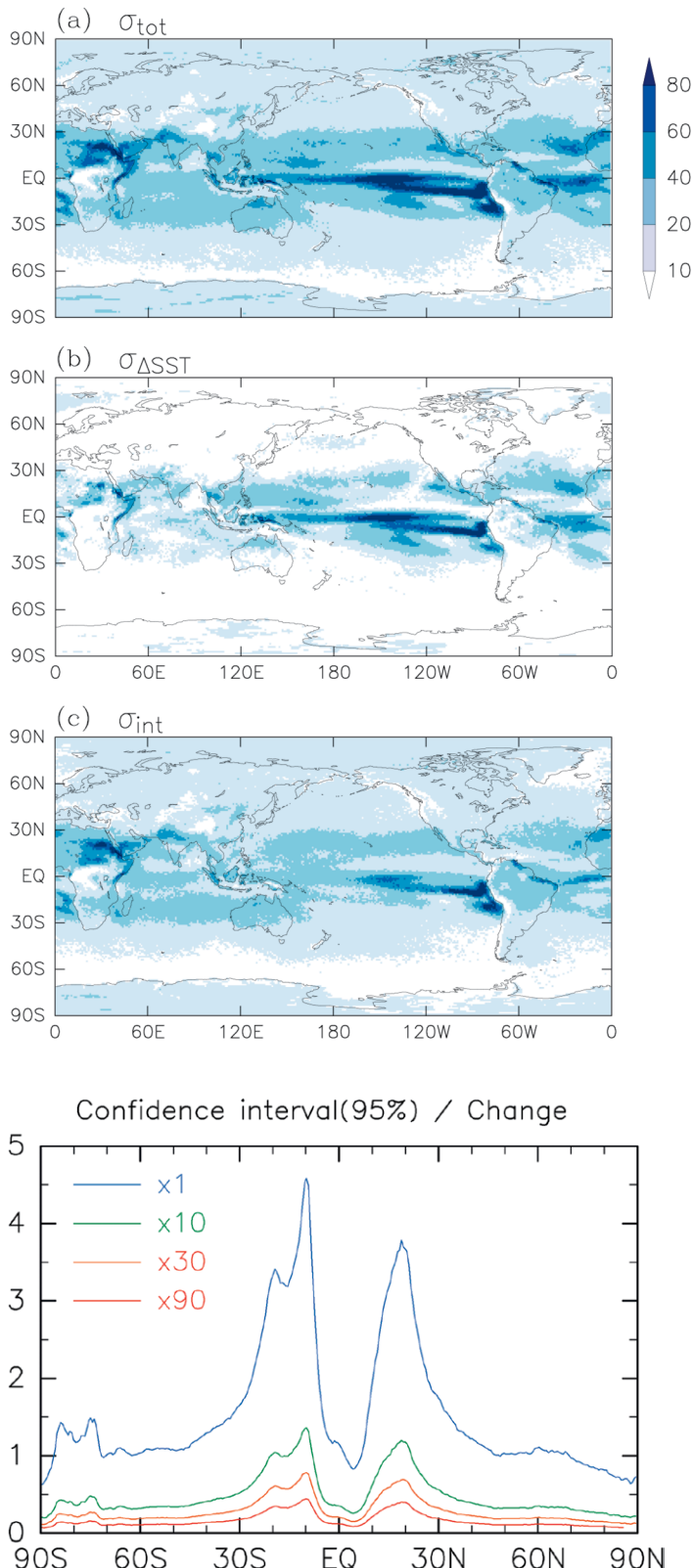


FIG. 6. Ratio of the zonal-mean 95% confidence interval of change to the zonal-mean change, for the 10-yr return value of daily precipitation. The confidence interval for N members is calculated from 90 sets of N -member ensembles chosen by the bootstrap method.

Such information on regional changes in extreme weather and climate events can be used to evaluate the impacts on natural disasters, agriculture, water resources, ecosystems, human health, and so on. In particular, very rare events with a return period of more than several decades must be evaluated for adaptation planning for flooding, sediment disasters, or high tides, since infrastructure such as dams and banks along rivers and coasts are constructed to prevent disasters caused by rare events. Figure 9 shows the 50-yr return value of surface wind speed. This return value is used for evaluating extremely high tide events. The distribution from the historical simulation (Fig. 9b) is smoother than that estimated from reanalysis data (Fig. 9a), which itself is useful for evaluating the distribution under the present climate. The change from the historical simulation to the +4-K simulation (Fig. 9c) shows an increase in the midlatitudes from 20° to 40°. A large part of the change is associated with the changes in the track and strength of tropical cyclones, which will also be reported in another publication.

BENEFITS OF THE HIGH-RESOLUTION

LARGE ENSEMBLE: RCM.

Extreme daily precipitation is projected using RCM simulations, which enable analyses of the detailed spatial distribution of extreme precipitation. Figure 10a shows the distribution of the 50-yr return value of daily precipitation around the main Japanese islands estimated from observational data. The return value is calculated using the maximum likelihood fitting for the generalized extreme value (GEV) distribution with the annual maximum daily precipitation (R1d) data. The results of the observational station data are interpolated onto the model land grid points. The value in the historical simulation is calculated in the same way to compare with that of the observation and is shown in Fig. 10b. The spatial distributions of the extreme precipitation in the model and observational results are similar to each other, with larger values on the coast of the Pacific Ocean. This is due to the high horizontal resolution of the RCM.

The future change is presented in Fig. 10c. Basic patterns of the changes are similar to the value in the

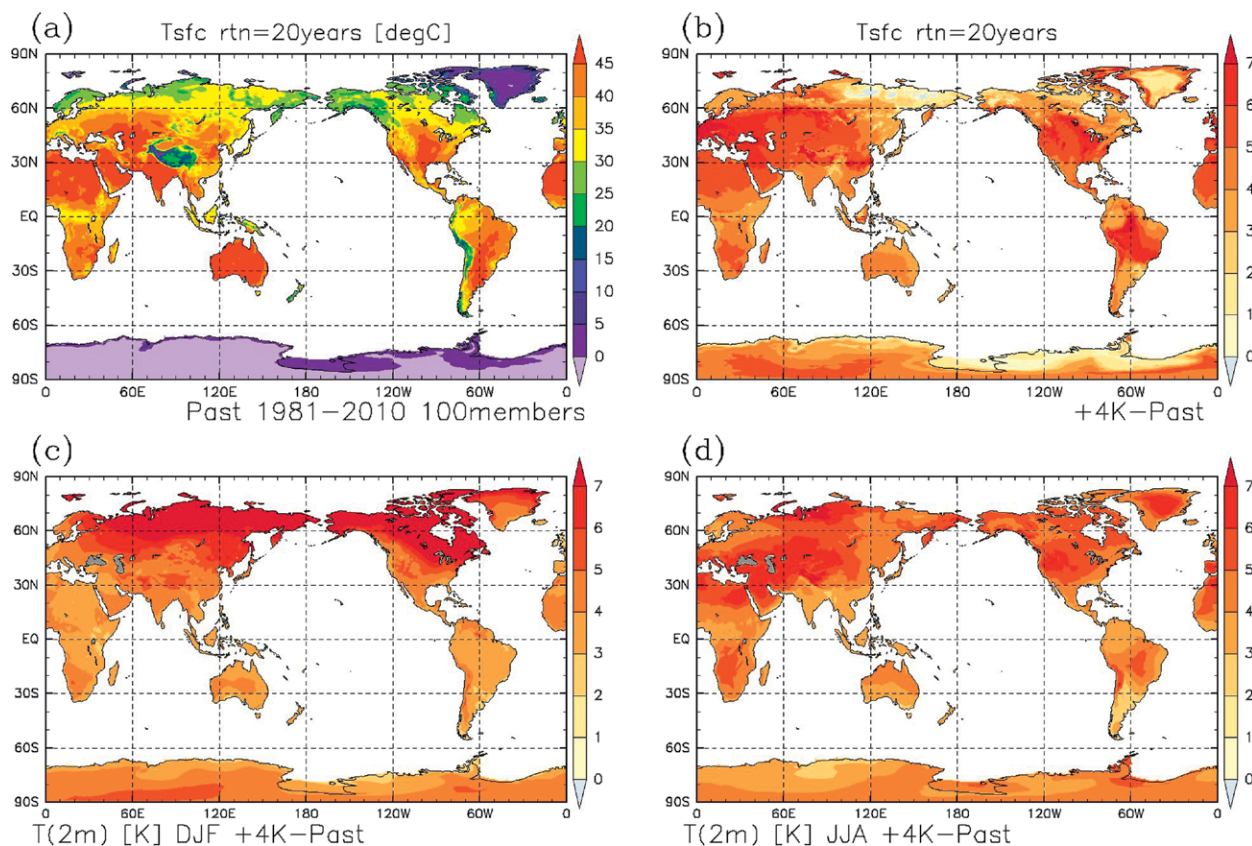


FIG. 7. (top) The 20-yr return value of maximum surface air temperature for (a) the latter half of the historical simulation and (b) the change in the +4-K simulation. These 20-yr return values are calculated from the 95th-percentile value of annual maximum of daily maximum temperature. (bottom) Seasonal-mean surface temperature change (c) from Dec to Feb and (d) from Jun to Aug.

historical simulation in Fig. 10b, which means the change relative to the value in the historical simulation has a larger spatial scale, especially along the coast of the Pacific Ocean (not shown). Whether the change in extreme precipitation is significant depends on the absolute values of the changes and their confidence intervals. Figure 10d shows the distribution of the 95% confidence intervals of the 50-yr-return-value estimation; these confidence intervals are the mean values of the historical and future simulations. The confidence intervals (Fig. 10d) are sufficiently smaller than the future changes (Fig. 10c) to conclude the significance of the future changes in most regions without a rigorous statistical test. This significance is due to the large number of samples, on the order of thousands, which reduces the confidence intervals and improves the reliability of estimations of extreme precipitation.

Next, extremely heavy precipitation in terms of annually accumulated precipitation is investigated. Annual amounts of precipitation are spatially averaged over each of the six regions of Japan shown in Fig. 11a and are sorted for each simulation. Then, the change in precipitation amount from the historical simulation to the +4-K simulation for each percentile is calculated. In this way, the dependence of changes in precipitation on percentile values is examined.

The change in the annually accumulated precipitation increases as the precipitation becomes heavier (Fig. 11b). For example, in the northern Japan (NJ) region the change ranges from 1.5% at the 5th percentile to 5.4% at the 95th percentile. This means that the amplitude of the variability increases in the future climate. This result is robust for the six regions of

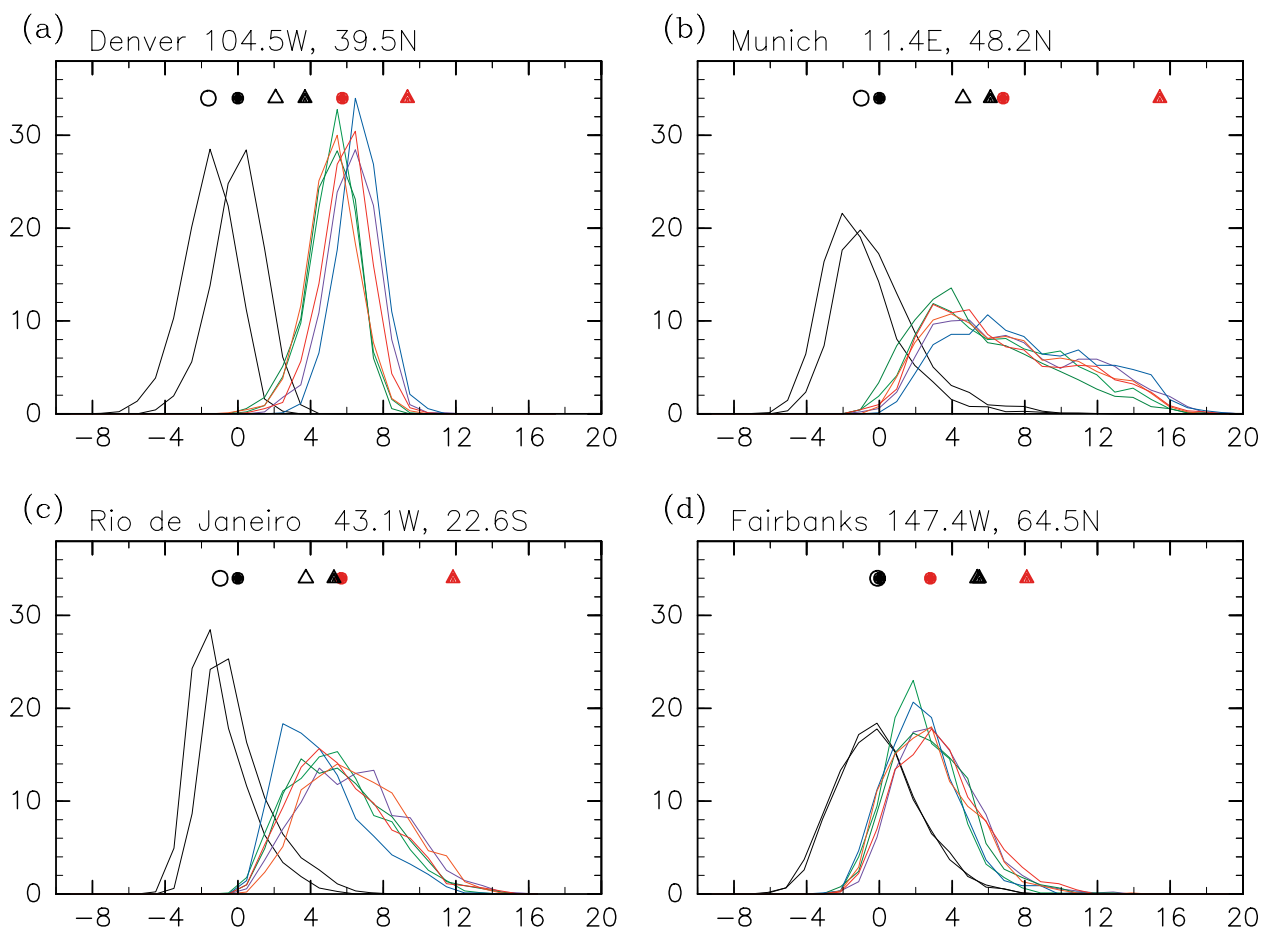


FIG. 8. Frequency distributions of annual maximum surface temperature for four representative points: (a) Denver (39.5°N, 104.5°W), (b) Munich (48.2°N, 11.4°E), (c) Rio de Janeiro (22.6°S, 43.1°W), and (d) Fairbanks (64.5°N, 147.4°W). The thick black line is from the latter half of the historical simulation, the thin black line is from the latter half of the nonwarming simulation, and color lines correspond to the six SST change patterns of the +4-K experiment. Bin size is 1 K, and the horizontal axis is the deviation from the average (K) in the latter half of the historical simulation. Circles and triangles are the averages and 20-yr return values, respectively, for the historical (black), nonwarming (open symbols), and +4-K (red) simulations.

Japan, except for below the 5th percentile and above the 95th percentile. The change tends to be negative for a range of lower percentiles in some regions. In the eastern (EJ) and western Japan (WJ) regions, the changes have negative values below about the 80th and 70th percentiles, respectively. Nevertheless, higher categories of the precipitation amount, such as the 90th percentile, increase even in those regions.

Thus, the increase in heavy precipitation, in the annually accumulated sense, is seen more broadly than the increase in mean precipitation.

DISCUSSION AND CONCLUDING REMARKS. Results of high-resolution large ensemble simulations with a 60-km global atmospheric model and a 20-km regional climate model

have been made publicly available as a database that enables us to discuss the uncertainty arising from internal variability in the future change in extreme weather and climate events. Using more than 5,000 years of data from the 60-km global model, extreme daily precipitation events with a return period of several decades can be calculated without any assumption of distribution functions. The increase in daily precipitation in the future simulation is greater for higher precipitation rates. Over central Europe and some other regions, the 20-yr return value of maximum surface temperature shows a greater increase than the mean temperature increase of the warm season. Using the downscaled results with the 20-km regional climate model, we obtain a more detailed spatial distribution associated with small topography.

The 60-km global model simulates realistic

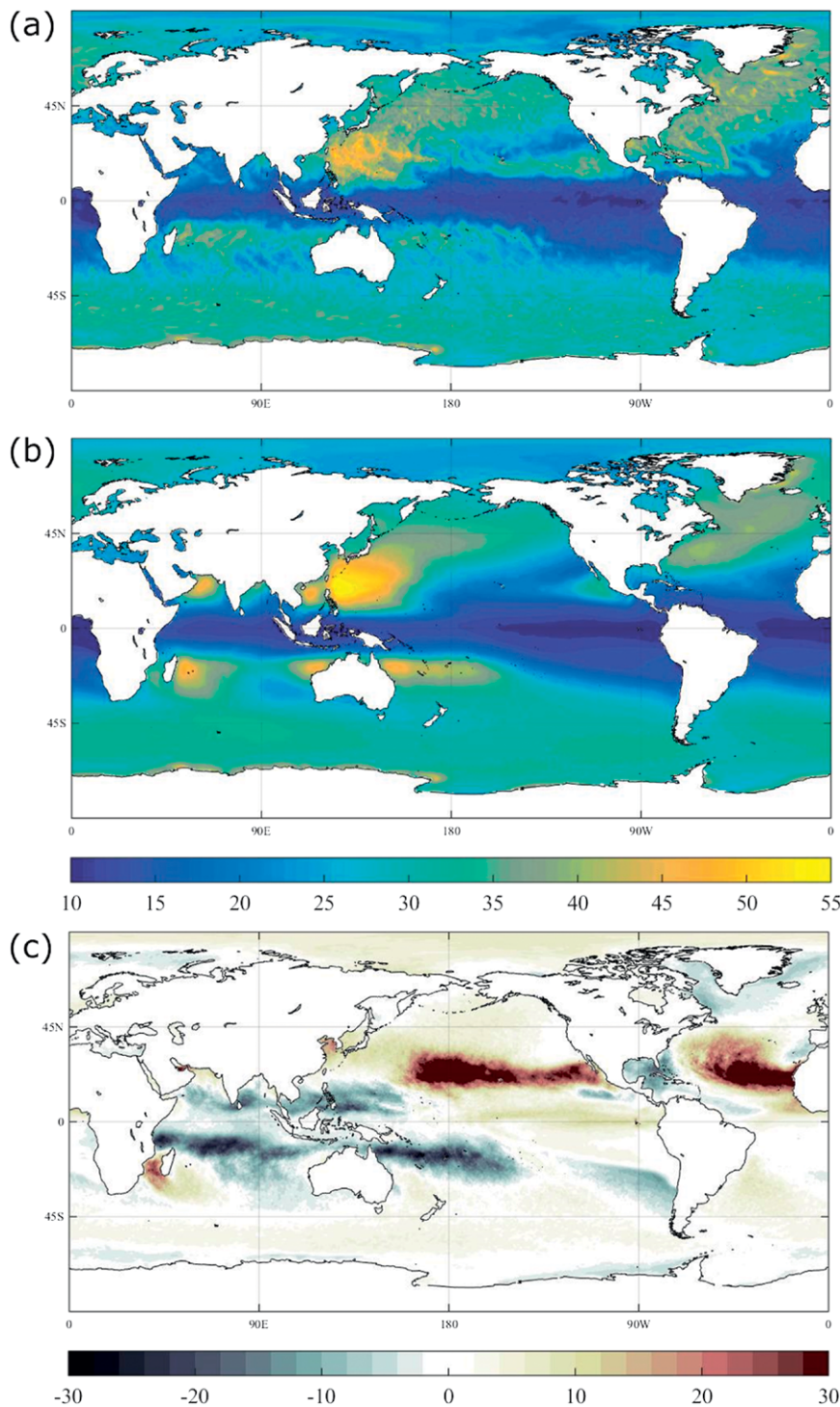


FIG. 9. Spatial distribution of the 50-yr return value of surface wind speed for (a) estimates from Japanese 55-year Reanalysis (JRA-55) data from 1958 to 2012 (m s^{-1}), (b) the historical simulation (m s^{-1}), and (c) the change from the historical simulation to the +4-K simulation (%).

tropical cyclones in terms of their global frequency distribution (Murakami et al. 2012b). Changes in, for instance, the spatial distribution of tropical cyclone frequency can be identified and will be reported in another paper. While intense tropical cyclones are not well represented due to the lack of horizontal resolution, their change can also be estimated by applying a bias correction.

The future experiment in the present study simulates the climate when the global-mean surface temperature becomes 4 K warmer than the preindustrial climate. The climate on the way to the 4-K warming is thought to be somewhere between the present climate and the +4-K climate. Whether “pattern scaling” can be applied, in which the change is estimated by linear interpolation of the global-mean surface temperature warming, would depend on the variables (Harris et al. 2013). We are planning to perform another experiment simulating a +2-K climate, which would enable us to estimate what variables are appropriate for pattern scaling.

Uncertainty in future change arising from the climate models is still large. For instance, the sign of the change in mean precipitation over the Maritime Continent region, which is related to patterns of SST change, depends on the climate models (Mizuta et al. 2014). In the present study, we are trying to consider the uncertainty by using different SST warming patterns from six different climate models. By doing so, we obtain different precipitation change patterns similar to those in the different climate models (Fig. 2). However, our results show a common distinctive pattern of change in summer precipitation over the northwestern Pacific different from the multimodel ensemble mean of the CMIP5 models. This is a limitation that arises from using the single MRI-AGCM. When similar high-resolution large ensemble simulations are performed by other models, an intercomparison would enable us to obtain more robust information on the probability of climate change. As an important step, outcomes from

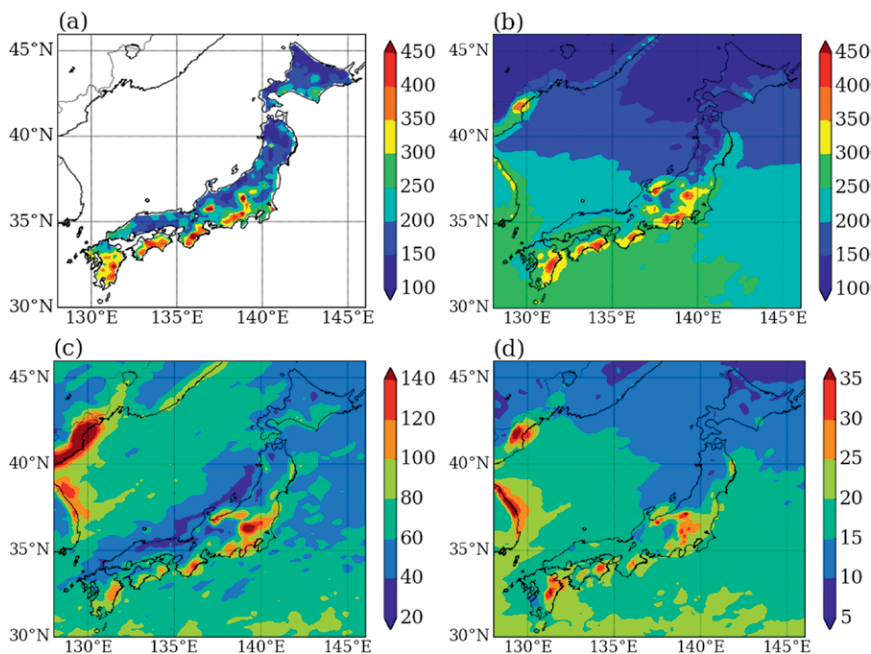


FIG. 10. Spatial distribution around the main Japanese islands of 50-yr return values of daily precipitation from (a) the historical climate model and (b) observational data [Automated Meteorological Data Acquisition System (AMeDAS) from 1980 to 1999], (c) difference between the historical and +4-K simulations, and (d) the average of the 95% confidence intervals in the historical and +4-K simulations.

the High Resolution Model Intercomparison Project (HighResMIP; Haarsma et al. 2016) would provide a chance to estimate the intermodel spread of the high-resolution simulations.

ACKNOWLEDGMENTS. The Earth Simulator supercomputer was used in this study under the “Strategic Project with Special Support” of JAMSTEC. The study was also supported by the Program for Risk Information on Climate Change (SOUSEI) and the Data Integration and Analysis System (DIAS), both of which are sponsored by the Ministry of Education, Culture, Sports, Science and Technology of Japan. Extreme values by the GEV method were calculated using the extRemes R package (Gilleland and Katz 2011). We thank two anonymous reviewers for the useful comments. The simulation results are available online (via <http://search.diasjp.net/search?lang=en&k=d4PDF>).

APPENDIX: PERTURBATIONS FOR THE ENSEMBLE EXPERIMENTS.

To obtain larger spreads of internal climate variability, perturbations of the lower boundary conditions are added for the ensemble simulations with the AGCM and the RCM, in addition to the use of different initial conditions. The initial conditions of the AGCM are

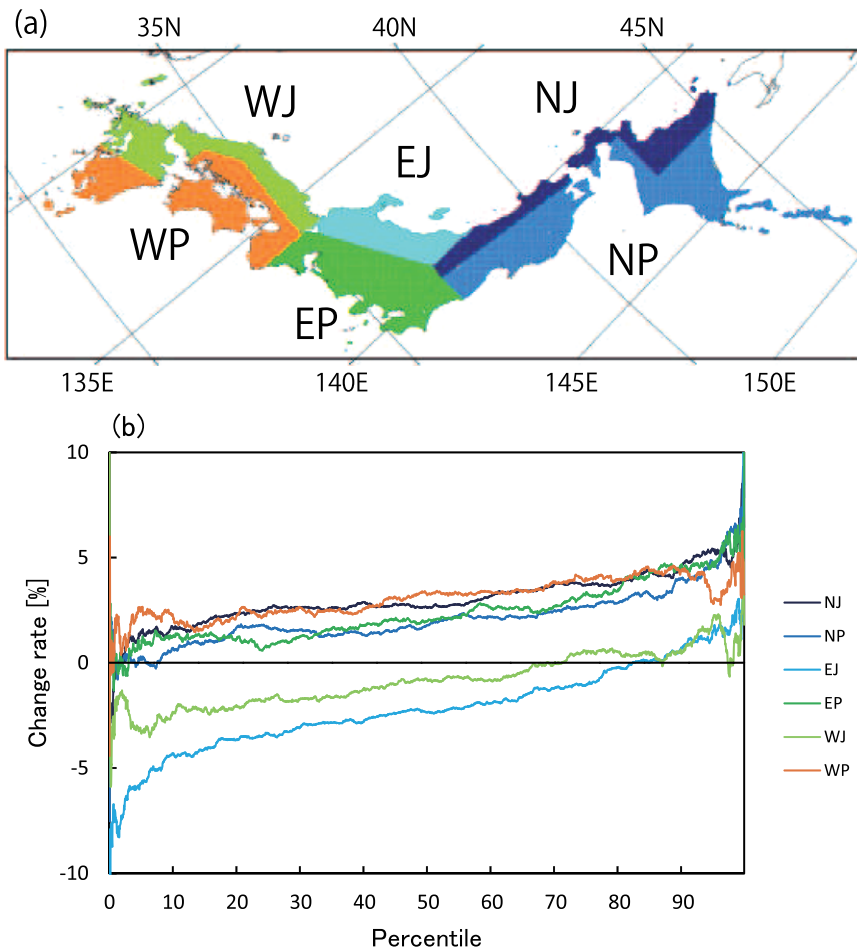


FIG. 11. (a) Map of Japan showing the regions used for analyses: Sea of Japan side of northern Japan (NJ), Pacific Ocean side of northern Japan (NP), Sea of Japan side of eastern Japan (EJ), Pacific Ocean side of eastern Japan (EP), Sea of Japan side of western Japan (WJ), and Pacific Ocean side of western Japan (WP). (b) Change in the annually accumulated precipitation averaged over each of the six regions. Data from 48 members for each simulation are used.

from snapshots on different dates in previous experiments with the same model, with 1 year of spinup. The perturbations of SST (δ SSTs) are constructed by using EOFs representing the interannual variations in SST. The EOFs are the same as those used for reconstructing historical SSTs (Hirahara et al. 2014). Here we assume that the true SST is completely represented by the EOFs and that the uncertainty in COBE-SST2 results solely from the sampling of SST observations. The time series of each EOF component for δ SST are randomly generated with an autoregressive moving-average model, assuming that the periodicity of each component is the same as that of the observations. The magnitude of the uncertainty should be proportional to the analysis errors that vary in space and time; however, this is set to be 30% of the standard deviation of the interannual variability

of SST uniformly in space and time so that historical changes in the observational network are removed from consideration when analyzing the model simulation outputs. The value of 30% has been used as a typical magnitude of SST uncertainty in recent decades. In addition, SST variations due to meso-scale oceanic eddy activity, which are not represented by the EOFs, are overlain on the abovementioned perturbed SST. The magnitude of the eddy contribution is defined as the root-mean-square difference between COBE-SST2 and a satellite SST analysis, the latter of which is included in the COBE-SST2 products. Eddy observations are available only in the satellite era, and hence artificial eddies are substituted using Gaussian noise smoothed on scales of 200 km in space and 30 days in time (Chelton et al. 2007).

The perturbations for SIC and SIT are also applied to the ensemble simulations, which are constructed consistently with δ SST. Using the relationship whereby SST is represented by quadratic functions of SIC (Hirahara et al. 2014), the SIC perturbation is inversely computed from δ SST. The coefficients of the functions vary with basin and season. Horizontal patterns of the SIC in the future simulations are calculated from the future SST using different coefficients, constructed from the future SST and SIC of the multimodel ensemble mean of 36 CMIP5 models for the period from 2080 to 2099. The equations satisfy the condition that the total sea ice extent in each hemisphere computed from the future climatological SSTs is the same as that of the future climatological SIC in the CMIP5 models. Different coefficients are used for the six Δ SSTs. This ensures that the total sea ice extent is close to that in the multimodel ensemble mean.

Also note that the perturbation of SIC is realized through the quadratic equations. The observed SIT climatology is multiplied by a constant factor for each hemisphere for the future SIT so that the hemispheric sea ice volume change is the same as that of the CMIP5 multimodel ensemble. Zero SIT is specified at a grid point where there is no sea ice.

It is confirmed that the ensemble AGCM experiments with the perturbed SST, SIC, and SIT show similar sizes of ensemble spread in the atmosphere to those by the experiments with only initial-value perturbations, except for atmospheric variables near the sea surface, which are highly correlated with the SST variations.

REFERENCES

- Allen, M. R., 2003: Liability for climate change. *Nature*, **421**, 891–892, doi:10.1038/421891a.
- Bourke, R. H., and R. P. Garrett, 1987: Sea ice thickness distribution in the Arctic Ocean. *Cold Reg. Sci. Technol.*, **13**, 259–280, doi:10.1016/0165-232X(87)90007-3.
- Chelton, D. B., M. G. Schlax, R. M. Samelson, and R. A. de Szoeke, 2007: Global observations of large oceanic eddies. *Geophys. Res. Lett.*, **34**, L15606, doi:10.1029/2007GL030812.
- Christidis, N., and P. A. Stott, 2014: Change in the odds of warm years and seasons due to anthropogenic influence on the climate. *J. Climate*, **27**, 2607–2621, doi:10.1175/JCLI-D-13-00563.1.
- Collins, M., and Coauthors, 2013: Long-term climate change: Projections, commitments and irreversibility. *Climate Change 2013: The Physical Science Basis*, T. F. Stocker et al., Eds., Cambridge University Press, 1029–1136.
- Deser, C., A. Phillips, V. Bourdette, and H. Teng, 2012: Uncertainty in climate change projections: The role of internal variability. *Climate Dyn.*, **38**, 527–546, doi:10.1007/s00382-010-0977-x.
- Deushi, M., and K. Shibata, 2011: Development of a Meteorological Research Institute Chemistry–Climate Model version 2 for the study of tropospheric and stratospheric chemistry. *Pap. Meteor. Geophys.*, **62**, 1–46, doi:10.2467/mripapers.62.1.
- Duong, D. T., Y. Tachikawa, and K. Yorozu, 2014: Changes in river discharge in the Indochina Peninsula region projected using MRI-AGCM and MIROC5 datasets. *J. Japan. Soc. Civil Eng. Ser. B1*, **70**, I_115–I_120.
- Endo, H., A. Kitoh, T. Ose, R. Mizuta, and S. Kusunoki, 2012: Future changes and uncertainties in Asian precipitation simulated by multiphysics and multi-sea surface temperature ensemble experiments with high-resolution Meteorological Research Institute atmospheric general circulation models (MRI-AGCMs). *J. Geophys. Res.*, **117**, D16118, doi:10.1029/2012JD017874.
- , —, R. Mizuta, and M. Ishii, 2017: Future changes in precipitation extremes in East Asia and their uncertainty based on large ensemble simulations with a high-resolution AGCM. *SOLA*, **13**, 7–12, doi:10.2151/sola.2017-002.
- Fowler, H., M. Ekstrom, S. Blenkinsop, and A. Smith, 2007: Estimating change in extreme European precipitation using a multimodel ensemble. *J. Geophys. Res.*, **112**, D18104, doi:10.1029/2007JD008619.
- Gilleland, E., and R. W. Katz, 2011: New software to analyze how extremes change over time. *Eos, Trans. Amer. Geophys. Union*, **92**, 13–14, doi:10.1029/2011EO020001.
- Haarsma, R. J., and Coauthors, 2016: High Resolution Model Intercomparison Project (HighResMIP v1.0) for CMIP6. *Geosci. Model Dev.*, **9**, 4185–4208, doi:10.5194/gmd-9-4185-2016.
- Harris, G. R., D. M. H. Sexton, B. B. Booth, M. Collins, and J. M. Murphy, 2013: Probabilistic projections of transient climate change. *Climate Dyn.*, **40**, 2937–2972, doi:10.1007/s00382-012-1647-y.
- Hawkins, E., and R. Sutton, 2009: The potential to narrow uncertainty in regional climate predictions. *Bull. Amer. Meteor. Soc.*, **90**, 1095–1107, doi:10.1175/2009BAMS2607.1.
- Hirahara, S., M. Ishii, and Y. Fukuda, 2014: Centennial-scale sea surface temperature analysis and its uncertainty. *J. Climate*, **27**, 57–75, doi:10.1175/JCLI-D-12-00837.1.
- IPCC, 2013: *Climate Change 2013: The Physical Science Basis*. Cambridge University Press, 1535 pp.
- JMA, 2007: Outline of the operational numerical weather prediction at the Japan Meteorological Agency; Appendix to WMO technical progress report. Japan Meteorological Agency, 194 pp. [Available online at www.jma.go.jp/jma/jma-eng/jma-center/nwp/outline-nwp/index.htm.]
- Kanada, S., M. Nakano, and T. Kato, 2012: Projections of future changes in precipitation and the vertical structure of the frontal zone during the Baiu season in the vicinity of Japan using a 5-km-mesh regional climate model. *J. Meteor. Soc. Japan*, **90A**, 65–86, doi:10.2151/jmsj.2012-A03.
- Kay, J. E., and Coauthors, 2015: The Community Earth System Model (CESM) Large Ensemble project: A community resource for studying climate change in the presence of internal climate variability. *Bull. Amer. Meteor. Soc.*, **96**, 1333–1349, doi:10.1175/BAMS-D-13-00255.1.

- Kharin, V. V., F. W. Zwiers, X. Zhang, and M. Wehner, 2013: Changes in temperature and precipitation extremes in the CMIP5 ensemble. *Climatic Change*, **119**, 345–357, doi:10.1007/s10584-013-0705-8.
- Kitoh, A., and H. Endo, 2016: Future changes in rainfall extremes associated with El Niño projected by a global 20-km mesh atmospheric model. *SOLA*, **12A**, 1–6, doi:10.2151/sola.12A-001.
- , T. Ose, and I. Takayabu, 2016: Dynamical downscaling for climate projection with high-resolution MRI AGCM-RCM. *J. Meteor. Soc. Japan*, **94A**, 1–16, doi:10.2151/jmsj.2015-022.
- Kusunoki, S., and R. Mizuta, 2013: Changes in precipitation intensity over East Asia during the 20th and 21st centuries simulated by a global atmospheric model with a 60 km grid size. *J. Geophys. Res. Atmos.*, **118**, 11 007–11 016, doi:10.1002/jgrd.50877.
- Mizuta, R., and Coauthors, 2012: Climate simulations using MRI-AGCM3.2 with 20-km grid. *J. Meteor. Soc. Japan*, **90A**, 233–258, doi:10.2151/jmsj.2012-A12.
- , O. Arakawa, T. Ose, S. Kusunoki, H. Endo, and A. Kitoh, 2014: Classification of CMIP5 future climate responses by the tropical sea surface temperature changes. *SOLA*, **10**, 167–171, doi:10.2151/sola.2014-035.
- Mori, M., M. Watanabe, H. Shiogama, J. Inoue, and M. Kimoto, 2014: Robust Arctic sea-ice influence on the frequent Eurasian cold winters in past decades. *Nat. Geosci.*, **7**, 869–873, doi:10.1038/ngeo2277.
- Mori, N., T. Yasuda, H. Mase, T. Tom, and Y. Oku, 2010: Projection of extreme wave climate change under the global warming. *Hydrol. Res. Lett.*, **4**, 15–19, doi:10.3178/hrl.4.15.
- Murakami, H., and Coauthors, 2012a: Future changes in tropical cyclone activity projected by the new high-resolution MRI-AGCM. *J. Climate*, **25**, 3237–3260, doi:10.1175/JCLI-D-11-00415.1.
- , R. Mizuta, and E. Shindo, 2012b: Future changes in tropical cyclone activity projected by multi-physics and multi-SST ensemble experiments using the 60-km-mesh MRI-AGCM. *Climate Dyn.*, **39**, 2569–2584, doi:10.1007/s00382-011-1223-x.
- Murata, A., H. Sasaki, M. Hanafusa, and K. Kurihara, 2013: Estimation of urban heat island intensity using biases in surface air temperature simulated by a nonhydrostatic regional climate model. *Theor. Appl. Climatol.*, **112**, 351–361, doi:10.1007/s00704-012-0739-2.
- Nakano, M., M. Matsueda, and M. Sugi, 2013: Future projections of heat waves around Japan simulated by CMIP3 and high-resolution Meteorological Research Institute atmospheric climate models. *J. Geophys. Res. Oceans*, **118**, 5461–5488, doi:10.1002/jgrc.20375.
- Pall, P., T. Aina, D. A. Stone, P. A. Stott, T. Nozawa, A. G. J. Hilberts, D. Lohmann, and M. R. Allen, 2011: Anthropogenic greenhouse gas contribution to flood risk in England and Wales in autumn 2000. *Nature*, **470**, 382–385, doi:10.1038/nature09762.
- Rowell, D. P., C. K. Folland, K. Maskell, and M. N. Ward, 1995: Variability of summer rainfall over tropical North Africa (1906–92): Observations and modelling. *Quart. J. Roy. Meteor. Soc.*, **121**, 669–704, doi:10.1002/qj.49712152311.
- Sasaki, H., A. Murata, M. Hanafusa, M. Oh'izumi, and K. Kurihara, 2011: Reproducibility of present climate in a non-hydrostatic regional climate model nested within an atmosphere general circulation model. *SOLA*, **7**, 173–176, doi:10.2151/sola.2011-044.
- Shimura, T., N. Mori, and H. Mase, 2015: Future projection of ocean wave climate: Analysis of SST impacts on wave climate changes in the western North Pacific. *J. Climate*, **28**, 3171–3190, doi:10.1175/JCLI-D-14-00187.1.
- Shiogama, H., M. Watanabe, Y. Imada, M. Mori, Y. Kamae, M. Ishii, and M. Kimoto, 2014: Attribution of the June–July 2013 heat wave in the southwestern United States. *SOLA*, **10**, 122–126, doi:10.2151/sola.2014-025.
- Sugiyama, M., H. Shiogama, and S. Emori, 2010: Precipitation extreme changes exceeding moisture content increases in MIROC and IPCC climate models. *Proc. Natl. Acad. Sci. USA*, **107**, 571–575, doi:10.1073/pnas.0903186107.
- Vautard, R., and Coauthors, 2014: The European climate under a 2°C global warming. *Environ. Res. Lett.*, **9**, 034006, doi:10.1088/1748-9326/9/3/034006.
- Xie, S.-P., and Coauthors, 2015: Towards predictive understanding of regional climate change. *Nat. Climate Change*, **5**, 921–930, doi:10.1038/nclimate2689.
- Yasuda, T., S. Nakajo, S. Kim, H. Mase, N. Mori, and K. Horsburgh, 2014: Evaluation of future storm surge risk in East Asia based on state-of-the-art climate change projection. *Coastal Eng.*, **83**, 65–71, doi:10.1016/j.coastaleng.2013.10.003.
- Yukimoto, S., and Coauthors, 2012: A new global climate model of the Meteorological Research Institute: MRI-CGCM3—Model description and basic performance. *J. Meteor. Soc. Japan*, **90A**, 23–64, doi:10.2151/jmsj.2012-A02.